polysaccharides

MDPI

Article

One-Pot Synthesis of Chitosan/Layered Double Hydroxide Composite and Its Sorption Properties Toward Hexavalent Chromium

Roman A. Golubev [1,2], Andreii S. Kritchenkov [1,2], Anton R. Egorov [1], Daria I. Semenkova [1,2], Linh V. Nguyen [1], Anatoly A. Kirichuk [1], Nikolai N. Lobanov [1], Alexander G. Tskhovrebov [1], Gunay Z. Mammadova [3], Aleh V. Kurliuk [4], Wanjun Liu [5] and Omar M. Khubiev [1,*]

[1] Department of Human Ecology and Bioelementology & Department of General and Inorganic Chemistry, Peoples' Friendship University of Russia Named After Patrice Lumumba, 6 Miklukho-Maklaya St, Moscow 117198, Russia; asdfdss.asdasf@yandex.ru (R.A.G.); kritchenkov-as@rudn.ru (A.S.K.); sab.icex@mail.ru (A.R.E.); darya.semenkova02@mail.ru (D.I.S.); linhno2109@gmail.com (L.V.N.); kirichuk-aa@rudn.ru (A.A.K.); lobanov-nn@rudn.ru (N.N.L.); alexander.tskhovrebov@gmail.com (A.G.T.)
[2] Institute of Technical Acoustics NAS of Belarus, Ludnikova Prosp. 13, 210009 Vitebsk, Belarus
[3] Organic Chemistry Department, Baku State University, Zahid Khalilov Street, 23, Baku Az 1148, Azerbaijan; gunka479@mail.ru
[4] Department of General and Clinical Pharmacology, Vitebsk State Medical University, Frunze Av. 27, 210009 Vitebsk, Belarus; aleh.kurliuk@gmail.com
[5] Shanghai Frontiers Science Center of Advanced Textiles, College of Textiles, Donghua University, Shanghai 201620, China; wjliuok@dhu.edu.cn
* Correspondence: ihubievomar1@gmail.com

Abstract

A one-pot strategy was developed for preparing a chitosan/Mg–Fe layered double hydroxide (LDH) composite by alkaline coprecipitation from an acidic chitosan solution containing Mg(II) and Fe(III) precursors, avoiding separate LDH synthesis and subsequent incorporation into chitosan. X-ray diffraction confirmed LDH formation within the chitosan matrix, and ICP analysis indicated an LDH-equivalent content of approximately 4.1 wt.% on an anhydrous basis. The composite exhibited enhanced chromate adsorption compared with both starting components. The experimental plateau adsorption capacity reached 137.4 mg/g, exceeding those of chitosan (92.2 mg/g) and Mg–Fe LDH (53.5 mg/g). Nonlinear isotherm fitting showed that Mg–Fe LDH was better described by the Freundlich model, whereas chitosan and the composite were better described by the Langmuir model. The kinetic behavior followed the pseudo-second-order equation, while Weber–Morris analysis indicated multistep uptake involving surface interaction and diffusion-related processes. In simulated groundwater containing chloride, bicarbonate, and sulfate, the composite removed 82% of Cr(VI) at 1.0 g/L. It also retained complete chromate uptake over five sorption/desorption cycles, although desorption efficiency decreased from 97.3% to 90.3%. A limitation of this study is that performance was evaluated mainly in batch systems and simplified simulated groundwater; validation with real contaminated waters and dynamic flow conditions is still required.

Keywords: chitosan; layered double hydroxides; hexavalent chromium; composites; sorption

Check for updates

Received: 30 March 2026
Revised: 8 May 2026
Accepted: 19 May 2026
Published: 21 May 2026

Copyright: © 2026 by the authors. Licensee MDPI, Basel, Switzerland. This article is an open access article distributed under the terms and conditions of the Creative Commons Attribution (CC BY) license.

1. Introduction

Polysaccharides are natural polymers that are highly attractive for modern, environmentally oriented materials science [1]. The use of polysaccharides in the development

of new functional polymer-based materials in recent years has resulted in an exciting growth in high-ranking publications and international patents, directly demonstrating the importance and relevance of the field [2–4]. Chitosan is a natural, non-toxic polysaccharide. It is a copolymer of D-glucosamine and N-acetyl-D-glucosamine. The mole fraction of D-glucosamine units in chitosan depends on the degree of deacetylation (DD) and typically ranges from approximately 60 to 90% [5]. Chitosan is a partially deacetylated derivative of chitin and is a renewable, biocompatible, biodegradable, and environmentally friendly polysaccharide, which makes it attractive for environmentally oriented materials science.

Layered double hydroxides (LDHs) are a broad class of inorganic compounds consisting of layers of di- and trivalent metal cations (M^{2+} and M^{3+}) linked by bridging hydroxide ligands. The interlayer space of the LDHs is filled with water molecules and anions (A^{n-}). This results in the general formula of layered double hydroxides $[M^{2+}{}_{1-x}M^{3+}{}_{x}(OH)_2]^{x+}(A^{n-})_{x/n} \times yH_2O$. Layered double hydroxides (LDHs) are also known as anionic clays. LDHs possess a rich intercalation chemistry which determines their anion-exchange properties. A significant advantage of LDHs is their ease and low cost of production [6]. LDHs also are attractive as catalysts [7,8], especially for those reactions that are not feasible without a metal center [9,10]. LDHs have also been employed as carriers not only for conventional drug molecules [11], but also for more unconventional guest systems, including water-soluble fullerene derivatives [12], the most prominent example being fullerenol [13], as well as diverse heterocyclic compounds [14–16], many of which are capable of forming strong intermolecular interactions [17].

Both chitosan and LDH are materials with attractive sorption properties. In particular, chitosan and its numerous derivatives have shown high sorption capacity for heavy metal ions [18–20], cationic and anionic organic dyes [21,22], pesticides [23], and a number of other environmentally hazardous pollutants [24]. LDHs are also known as effective sorbents mainly for anionic compounds [25], but are also capable of sorbing cationic compounds, such as uranyl ion [26], selenium oxo-anions [27], parabens [28], 2,4-dichlorophenol [29], dyes [30], and many other environmentally hazardous pollutants. Not surprisingly, in recent years, several composite sorbents have been obtained in which LDHs act as a filler distributed in a chitosan polymer matrix [27,28,31–33]. More recent studies from 2022–2025 further confirm the rapid development of chitosan–LDH composite sorbents. Examples include CoAl-LDH@chitosan/Fe_3O_4 for Pb(II) and Cr(VI) adsorption [32], Mg–Al LDH/chitosan and M^{2+}/Al LDH–chitosan composites for anionic dye adsorption [30,34], chitosan–LDH composites prepared on chitosan microspheres and LDH/chitosan composites for anionic dye removal [31,35], and LDH encapsulated with chitosan hydrogel-type sorbents [36,37]. Recent LDH-based systems for Cr(VI) adsorption also confirm the continuing relevance of LDH-containing materials for hexavalent chromium removal [38,39].

Papers focusing on the synthesis and characterization of chitosan-LDH composites describe composite preparation as a two-step process: (1) LDH synthesis and (2) LDH introduction into a chitosan solution, followed by precipitation and drying. In recent work, the post-synthetic incorporation of preformed LDH into chitosan matrices has generally been implemented through mixing, coating, encapsulation, crosslinking, or magnetic composite formation; these routes are effective but remain multistep and require separate preparation and handling of LDH particles. Chitosan is insoluble in organic solvents and is soluble only in water at acidic pH values. The introduction of LDH into an acidic chitosan solution should inevitably lead to partial destruction of the hydroxide structure by the acid, which is a significant drawback of this method. Thus, the limitation of previous strategies is not the formation of chitosan-LDH composites per se, but the absence of a single-stage procedure in which LDH particles are generated directly inside the chitosan-containing

medium under alkaline coprecipitation conditions. However, the literature lacks data on a logical alternative approach to obtaining chitosan-LDH composites. In our opinion, such an approach would involve adding alkali to an acidic chitosan solution containing LDH precursors (soluble di- and trivalent metal salts), which logically should result in the in situ formation of small LDH particles and their coprecipitation with chitosan. We hypothesize that this approach will avoid damaging the hydroxide structure of LDH and will be significantly more convenient due to its single-step nature. The novelty of the present work lies in the direct one-pot in situ coprecipitation of Mg–Fe LDH within a chitosan matrix, rather than in a conventional physical combination of preformed LDH with chitosan. Therefore, in this study, we explored the potential of the proposed approach for synthesizing a chitosan composite with magnesium-iron LDH and investigated the sorption capacity of the resulting composite for chromate ions, i.e., hexavalent chromium, a hazardous environmental pollutant. We present a detailed discussion of the experiments and their results in the sections that follow below.

2. Materials and Methods

Crab chitosan (Glentham, Corsham, UK), magnesium nitrate hexahydrate, iron(III) nitrate nonahydrate, potassium chromate, and sodium hydroxide (Sigma Aldrich, St. Louis, MO, USA) were used in this study. Other reagents and solvents were obtained from commercial sources and used without further purification.

Mg/Fe LDH was prepared using the standard unified [40] method, differing only in that we used 12.82 g $Mg(NO_3)_2 \times 6H_2O$ instead of 19.23 g in order to achieve a Mg/Fe ratio of 2/1.

Composite synthesis: 1.00 g of chitosan was dissolved in 30 mL of 1% acetic acid for 12 h with vigorous stirring. 0.100 g of magnesium nitrate hexahydrate and 0.0790 g of iron nitrate nonahydrate, dissolved in 10 mL of distilled water, were added to the resulting solution and stirred for 5 h. A solution of 0.30 g of sodium hydroxide in 10 mL of water was added dropwise over 10 min under vigorous stirring and pulsed ultrasound treatment. The resulting precipitate was separated by centrifugation, washed with distilled water to a neutral pH, dispersed in 15 mL of distilled water and lyophilized.

To study sorption equilibria, 0.150 g of sorbent was added to 12.00 mL of potassium chromate solution with concentrations ranging from 0.04046 to 2.1577 g/L. The reaction mixture was stirred at 293 K for 24 h and then centrifuged. The concentration of Cr(VI) in the supernatant was determined spectrophotometrically at 540 nm according to Vogel's classical method for chromate/hexavalent chromium determination [41]. This method was selected because it allows selective determination of Cr(VI), whereas atomic absorption spectroscopy determines total chromium unless additional speciation procedures are used. We used KFK-3 UV-Vis spectrophotometer with a 1 cm optical path length cuvette. Before measurements, calibration curves were prepared using standard K_2CrO_4 solutions in the relevant concentration range. Blank correction was applied, and only calibration curves with satisfactory linearity were used for quantitative determination. The equilibrium adsorption values q_e were calculated from the difference between the initial and equilibrium Cr(VI) concentrations according to the mass-balance equation: $q_e = (C_0 - C_e)V/m$, where C_0 is the initial Cr(VI) concentration, C_e is the equilibrium Cr(VI) concentration after sorption, V is the solution volume, and m is the mass of the sorbent. The experimental Q_{max} value was determined as the maximum q_e value reached in the plateau region of the adsorption isotherm.

To study the kinetics of sorption processes, 0.150 g of sorbent was added to 150.00 mL of K_2CrO_4 solution with an initial Cr(VI) concentration of 20 mg/L. The suspension was stirred at 298 K for 60 min. Aliquots of the suspension were taken at fixed time intervals of

2, 3, 4, 10, 15, 30, and 60 min. The sorbent particles were separated from the liquid phase by centrifugation, and the residual Cr(VI) concentration in the supernatant was determined spectrophotometrically at 540 nm using Vogel's classical method for chromate/hexavalent chromium determination [41]. The absorbance measurements were performed using a KFK-3 UV-Vis spectrophotometer with a 1 cm optical path length cuvette. The adsorption value at time t, q_t, was calculated according to the following equation: $q_t = (C_0 - C_t)V/m$, where C_0 is the initial Cr(VI) concentration, C_t is the Cr(VI) concentration at time t, V is the solution volume, and m is the mass of the sorbent.

The pH of the chromate solutions was measured before and after sorption experiments using a calibrated pH meter. No additional pH adjustment was performed during the sorption experiments. The pH values were in the range of 6.93–7.18 for both the equilibrium and kinetic studies. All adsorption experiments were performed in triplicate.

^{1}H NMR spectra were recorded at the RUDN University Research and Educational Center using a JNM-ECA 600 spectrometer (JEOL, Tokyo, Japan, operating frequency 600 MHz, D_2O, CF_3COOH). ^{1}H NMR spectroscopy was used to calculate the degree of deacetylation of chitosan based on the ratio of the integral intensities of the signals of different protons (for proton numbering, see Figure 1):

$$DD(\%) = 1 - \left(\frac{I_{CH_3}}{3}\right) / \left(\frac{I_{H_2-H_6}}{6}\right),$$

where I_{CH3} is integral intensity *N*-acetyl protons, I_{H2-H6} is sum of integral intensities $H_{2,3,4,5,6}$ protons.

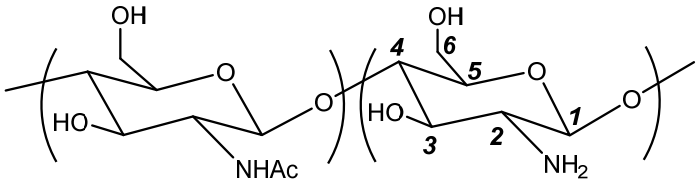


Figure 1. Structural formula of chitosan with proton numbering.

Fourier-transform infrared spectra were recorded using an INFRASPEC FSM 2202 Fourier-transform infrared spectrometer (Infraspec, Saint Petersburg, Russia) with an ATR attachment in the range of 500–4000 cm^{-1}. Fourier-transform infrared spectra were used for quantitative determination of the degree of deacetylation. The degree of deacetylation of chitosan (DD) was calculated by the following empirical equation [42–44]:

$$DD(\%) = 100 - \left(31.92 \times \frac{A(Amid(I))}{A(Amid(II))} - 12.20\right)$$

and

$$DD(\%) = 100 - \frac{\left(\frac{A_{1318}}{A_{1420}} - 0.3822\right)}{0.03133}$$

Molecular weight of chitosan

In accordance with the above equations, we calculated the values of viscometric constants for the starting chitosan $k = 6.589 \times 10^{-3}$ (mL/g) or 6.589×10^{-5} (dL/g); $\alpha = 0.88$.

The viscosity-average molecular weight of chitosan was determined by capillary viscometry using glass viscometer VPZh-2 (d = 0.99 mm, K = 0.11962 mm^2/s^2) according to the method reported by Wang et al. [45]. The measurements were performed in 0.2 M CH_3COOH/0.1 M CH_3COONa at 30 °C using chitosan solutions with an initial concentration of 0.20 g/dL. The relative viscosity was calculated from the flow times of the polymer solution and the

solvent, and the reduced viscosity was plotted as a function of chitosan concentration. The intrinsic viscosity [η] was obtained by extrapolation of η_{sp}/C to zero concentration.

The viscosity-average molecular weight (M_η) was calculated using the Mark–Houwink–Sakurada equation:

$$[\eta] = KM\eta^{\alpha},$$

where K and α are viscometric constants. For chitosan dissolved in 0.2 M CH_3COOH/0.1 M CH_3COONa at 30 °C, these constants were calculated as a function of the degree of deacetylation according to Wang et al. [45]:

$$k = 1.64 \times 10^{-30} \times (DD\%)^{14}\ (mL/g);$$

$$\alpha = -1.02 \times 10^{-2} \times (DD\%) + 1.82,$$

where DD% is the degree of deacetylation expressed in percent.

X-ray phase analysis was performed at the RUDN University Physical Chemistry and Chemical Institute Shared Use Center on a Tongda TDM-20 automatic X-ray diffractometer (Dandong Tongda Science & Technology Co., Ltd., Dandong, China) in step-scan mode (2θ angle range of 5° ÷ 50° with a scanning step of Δ2θ = 0.02°, exposure time of 3 s, Cu Kα radiation). Differential thermal/thermogravimetric analysis was performed on a TA Instruments SDT Q600 (TA Instruments, New Castle, DE, USA) in ceramic crucibles at a heating rate of 10 °C/min over a temperature range of 30 to 600 °C.

In simulated groundwater experiments, the composition of the simulated groundwater (SO_4^{2-}, Cl^-, HCO_3^-) was based on natural groundwater from Aprelevka (Moscow Region, Russia). The simulated groundwater was obtained by dissolving $CaCl_2 \times 2H_2O$ (103 mg), $MgSO_4 \times 7H_2O$ (64 mg), and sodium bicarbonate (70 mg) in 500.00 mL of distilled water. Simulated groundwater or distilled samples (1000 mL) were charged with 16 mg of K_2CrO_4 and 0.2, 0.5, or 1.0 g of composite chitosan/LDH. The sorption flasks were then gently shaken for 2 h at 293 K, followed by quantitative determination of hexavalent chromium spectrophotometrically at 540 nm using the method.

For recyclability assessment, 0.500 g of the chitosan/LDH composite was placed in a K_2CrO_4 solution (500.0 mL, 10 mg/L) and shaken at 293 K for 2 h, followed by quantitative determination of hexavalent chromium spectrophotometrically at 540 nm using the method described above [41]. The chitosan/LDH composite was removed from the sorption mixture and treated by 500 mL of NaOH solution (1 mol/L) for 2 h at 293 K, followed by quantitative determination of hexavalent chromium as mentioned above.

Data treatment for adsorption isotherms and kinetic curves was performed by nonlinear least-squares fitting. The fit quality was evaluated using RMSE and R^2 values calculated in the original experimental scales.

3. Results and Discussion

3.1. Characterization of Chitosan

In the first stage of this study, we thoroughly characterized the starting chitosan, as we intended to compare its sorption capacity with that of the chitosan/LDH composite. For this characterization, we used IR spectroscopy, 1H NMR spectroscopy, viscometric analysis, and X-ray diffraction.

The IR spectrum of the starting chitosan contains characteristic bands of the stretching vibrations of hydroxyl groups and primary amino groups (ν_{OH} and ν_{NH} vibrations) at 3285 and 3356 cm^{-1}, as well as stretching vibrations of C–H bonds at 2869 cm^{-1}, which are typical for chitosan. The characteristic Amide I and Amide II bands appear at 1590 and 1652 cm^{-1}. The IR spectrum also displays the C–O–C vibration bands of the pyranose

ring at 1060, 1024, and 989 cm^{-1}. The characteristic band of deformation vibrations of the hydroxyl groups appears at 1373 cm^{-1}, while wagging vibrations of the CH_2 moiety give the band at 1318 cm^{-1}. The IR spectrum of the starting chitosan is shown in Figure 2. The assignment of characteristic bands to the corresponding characteristic groups in the IR spectrum of chitosan is presented in Table 1.

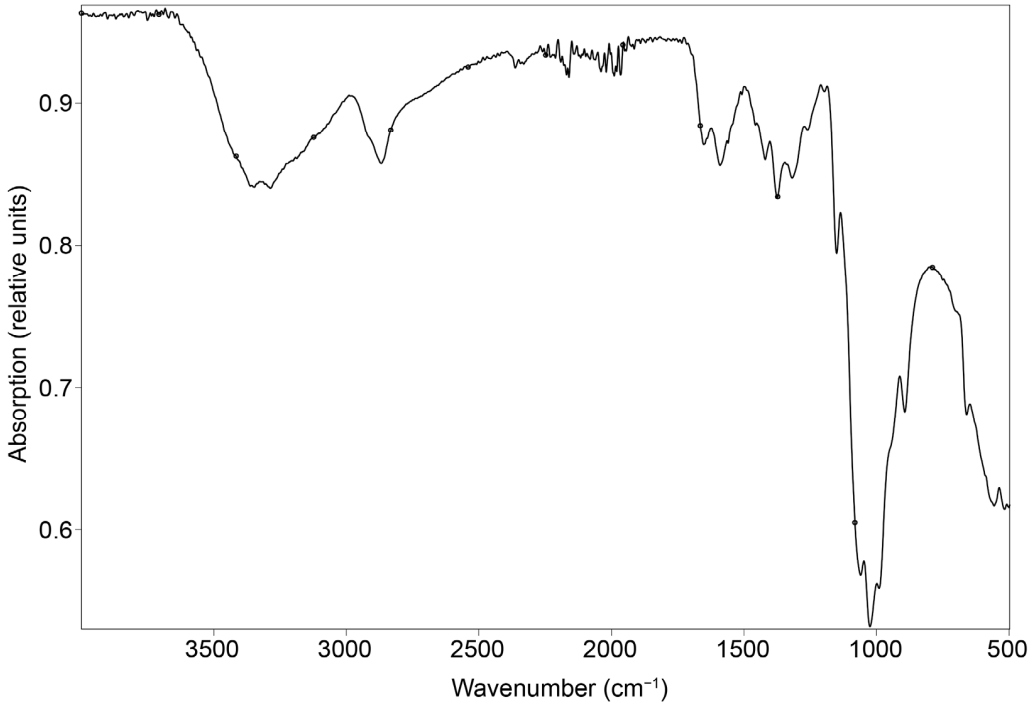


Figure 2. IR spectrum of chitosan.

Table 1. Correspondence of characteristic bands in the IR spectrum of chitosan to characteristic groups.

Vibration of the Characteristic Group	Maximum Absorption Band, cm^{-1}
$\omega_{C\text{-}H}$	893
Cycle C–O–C Cycle –OH	985, 1024, 1059
$\nu_{C–O}$	1150
ω_{CH2}	1320
$\delta_{O–H}$	1375
$\delta_{C–H}$	1419, 1454
$\delta_{N–H}$	1542, 1589
$\nu_{C=O}$	1649
ν_{CH}	2868, 2914
ν_{OH} и ν_{NH}	3291, 3352

IR spectroscopy can be successfully used to determine the degree of deacetylation (DD) of chitosan by empirical equations described in Section 2. For the starting chitosan, the degree of deacetylation calculated using both empirical equations was about 92%.

^{1}H NMR spectroscopy can also be used to determine the degree of deacetylation of chitosan [46,47].

The starting chitosan was also characterized by ^{1}H NMR spectroscopy. Figure 3 displays the ^{1}H NMR spectrum of chitosan with proton assignment, while Figure 1 displays its formula with proton numbering. The results of NMR spectroscopic analysis also indicate a degree of deacetylation of the starting chitosan of approximately 92–93%.

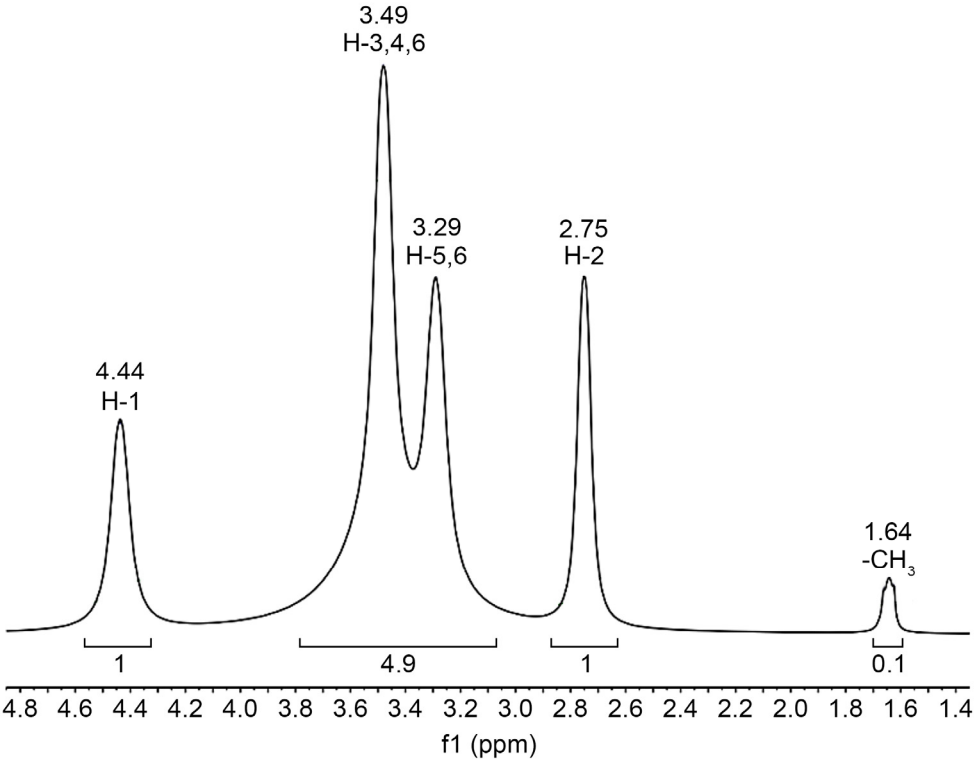


Figure 3. NMR spectrum of the starting chitosan.

Viscometry is one of the simplest methods in terms of equipment requirements and, at the same time one of the most informative for determining the molecular weight of a polymer [48]. According to the empirical equations relating the degree of deacetylation to the viscometric constants (see Section 2), we calculated the values of constants k and α for the starting chitosan (k = 6.589 $\times$ 10^{-3} (mL/g) or 6.589 $\times$ 10^{-5} (dL/g); α = 0.88). Table 2 and Figure 4 show the results of the viscometric study, and we used them to calculate the viscosity-average molecular weight of the starting polymer.

Table 2. Viscometric parameters of the chitosan solution.

№	V, mL	V_0, mL	V_{sum}, mL	τ_0, s	τ_i, s	η_{rel}	η_{sp}	η_{sp}/C, dL/g	C, g/dL
1	15	0	15	9.268	19.734	2.13	1.13	5.65	0.200
2	13	2	15	9.268	17.950	1.94	0.94	5.41	0.173
3	11	4	15	9.268	16.015	1.73	0.73	4.96	0.147
4	9	6	15	9.268	14.495	1.56	0.56	4.70	0.120
5	7	8	15	9.268	13.023	1.41	0.41	4.34	0.093
6	5	10	15	9.268	11.795	1.27	0.27	4.09	0.067
7	3	12	15	9.268	10.539	1.14	0.14	3.43	0.040

As a result of processing the experimental data, we found that the graph of the dependence of the reduced viscosity on the concentration of the chitosan solution is linear, and this allows us to determine the value of the intrinsic viscosity [η] by extrapolating according to condition $\frac{\eta_{sp}}{C}$ = [η] at C$\rightarrow$0. Thus, based on the experimental data, we found that [η] $\approx$ 3.0623 dL/g. According to the Mark–Kuhn–Houwink–Sakurada equation, we calculated the average viscosity molecular mass M_η = 201,219 Da $\approx$ 200 kDa.

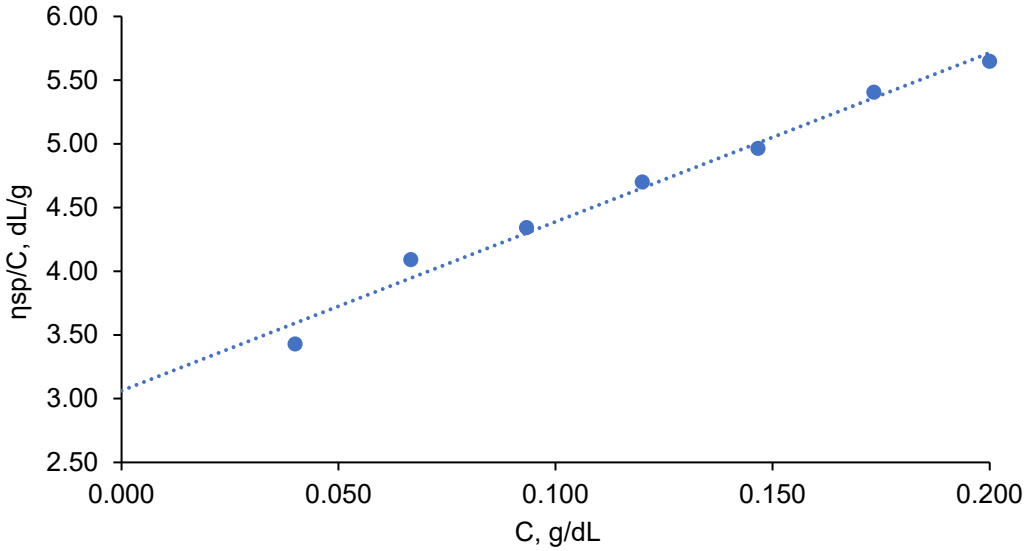


Figure 4. Dependence of reduced viscosity on the concentration of chitosan solution.

3.2. Synthesis of LDH

The hypothesis of this work was not only that coprecipitation from a chitosan solution containing magnesium and iron(III) ions by adding alkali would result in the formation of a chitosan/LDH composite, but also that the resulting composite would exhibit improved sorption properties compared to the starting chitosan and so-called "pure" LDH. To conduct the planned comparison, we synthesized "pure" magnesium-iron LDH The Mg/Fe ratio of 2.07 in the resulting LDH was confirmed by inductively coupled plasma mass spectrometry and was close to the desired Mg/Fe ratio of 2. X-ray phase analysis confirmed the formation of LDH, since the diffraction pattern of the obtained LDH (Figure 5) contains a set of basal reflections typical for this class of compounds and is fully consistent with the literature data [40] (basal reflections from planes (003), (006), (009), (012), (015)).

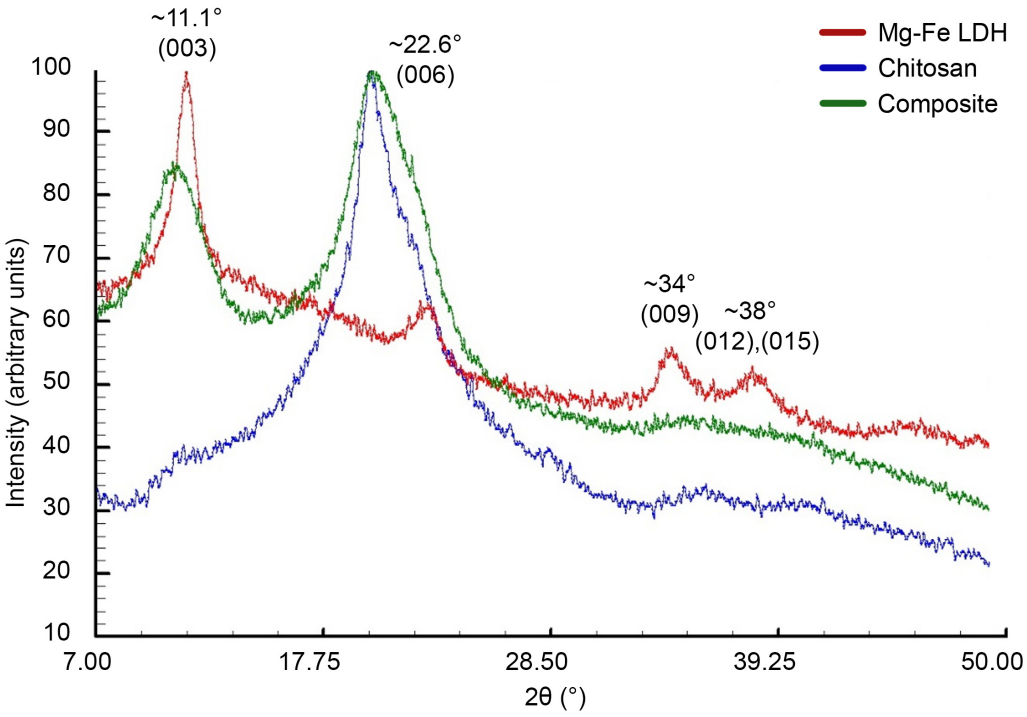
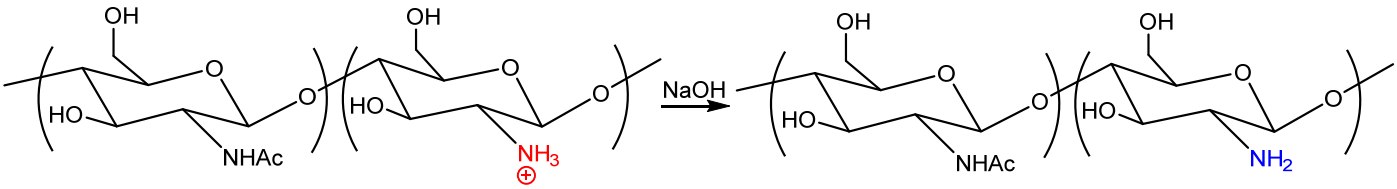


Figure 5. X-Ray diffraction pattern of a chitosan composite with magnesium-iron LDH.

3.3. Preparation and Characterization of Chitosan Composite with Magnesium-Iron LDH

We prepared the chitosan composite with magnesium-iron LDH by coprecipitation, which results in two parallel processes:

(i) the conversion of chitosan from a soluble salt form to an insoluble base form (Scheme 1);



Scheme 1. Conversion of chitosan from salt form to base form.

(ii) the formation of an insoluble magnesium-iron LDH:

$$2Mg^{2+} + Fe^{3+} + 6OH^- + NO_3{}^- + nH_2O = [Mg_2Fe(OH)_6](NO_3) \times nH_2O$$

The resulting composite sample is characterized by visual macroscopic homogeneity and is a yellow-cream-colored porous material (Figure 6).

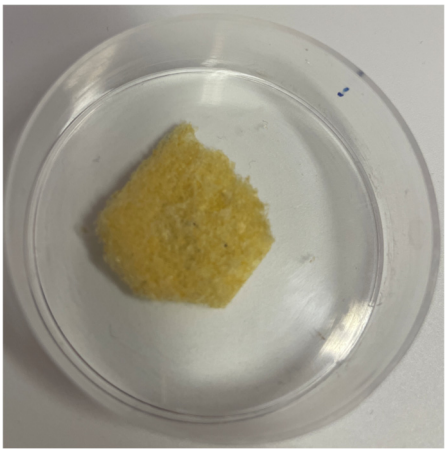


Figure 6. Appearance of a chitosan composite with magnesium-iron LDHs.

We confirmed the presence of the LDH phase in the chitosan polymer matrix using X-ray diffraction analysis. The diffraction pattern of the resulting composite (Figure 5) displays a broad peak characteristic of chitosan in the 2θ angle range from 19° to 22° corresponding to reflections ((200) and (201)) [49], as well as peaks characteristic of magnesium-iron LDH, i.e., an intense peak at ca. 11.1° 2θ (reflection (003)), a peak as an asymmetric shoulder in the region of 22.6° 2θ (reflection (006)) and broader, less resolved signals at higher 2θ° values ~34° and 38° 2θ corresponding to reflections (009) and (012), (015) [50].

IR spectroscopy also confirms the composition of the resulting composite. The IR spectrum (Figure 7) exhibits bands characteristic of chitosan, as well as bands typical of LDH: stretching vibrations of the nitrate ion at 1350 cm^{-1}, deformation vibrations of the water molecule at 1640 cm^{-1}, and characteristic vibrations of the metal–oxygen bond in the long-wavelength region of the spectrum (522 cm^{-1}).

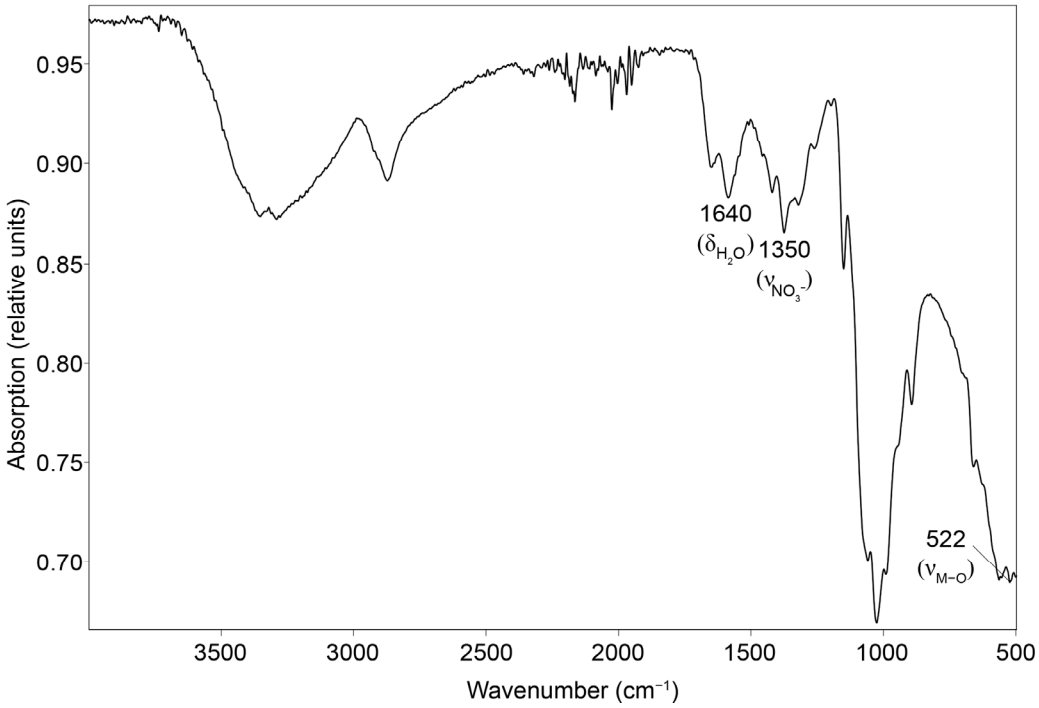


Figure 7. IR spectrum of a chitosan composite with magnesium-iron LDH.

The TGA and DSC curves of the resulting chitosan/Mg–Fe LDH composite are shown in Figure 8.

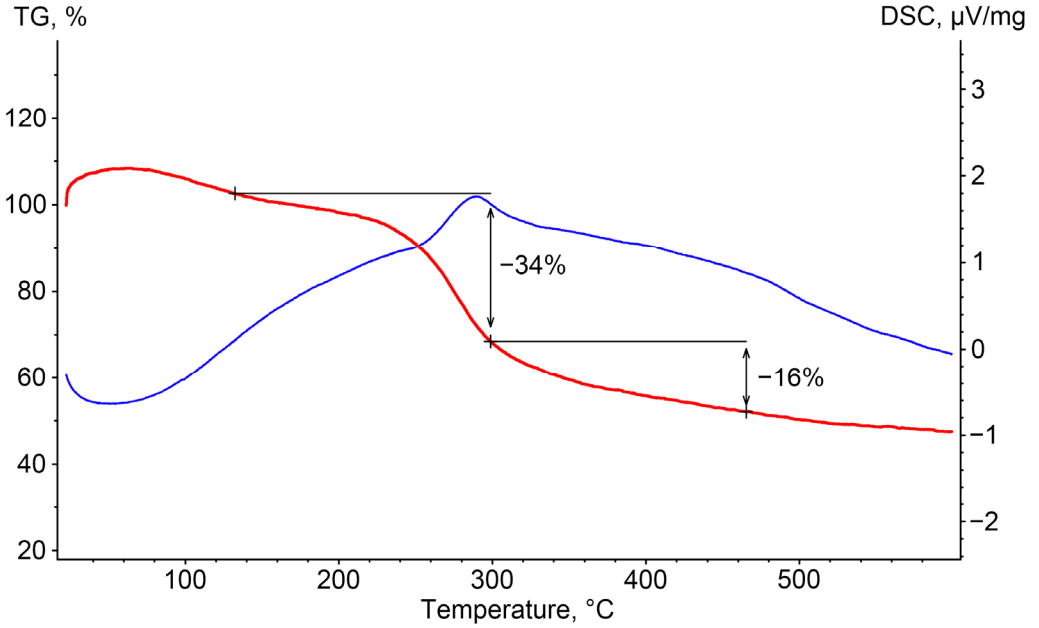


Figure 8. TGA(red)/DSC(blue) curves of a chitosan composite with magnesium-iron LDH.

The apparent increase in mass observed below 100 °C should not be interpreted as a real mass-gain process or as a chemical transformation in the sample. Since no distinct DSC event is observed in this temperature region, this feature is most likely related to instrumental effects at the initial stage of the TG experiment. Therefore, this region was excluded from the mechanistic interpretation of the composite degradation.

The thermal behavior of pristine chitosan has been extensively described in the literature. Typically, chitosan exhibits an initial low-temperature mass loss associated with the removal of physically adsorbed and bound water, followed by the main degradation of

the polysaccharide matrix beginning at approximately 240–250 °C and extending through the 250–350 °C region. This degradation includes dehydration, depolymerization, deacetylation, and cleavage of glycosidic bonds. These features of chitosan thermal degradation are consistent with previous TG/DSC and TG-coupled studies of chitosan [51–54]. In the present chitosan/Mg–Fe LDH composite, the thermal degradation proceeds mainly in two mass-loss stages. The first major mass-loss stage, observed at approximately 250–320 °C, can be attributed predominantly to the thermal degradation of the chitosan matrix. The second, more gradual mass-loss stage at higher temperatures is associated with further decomposition and carbonization of the organic residue, together with thermal transformations of the LDH component, including dehydroxylation of the hydroxide layers and decomposition/removal of interlayer nitrate species. Such multistep thermal behavior is typical for LDH-containing systems, in which dehydration, dehydroxylation, and interlayer-anion removal may occur in overlapping temperature regions [55]. The mass losses in these two regions were approximately 34% and 16%, respectively. Compared with pristine chitosan, the chitosan/Mg–Fe LDH composite exhibits a broader degradation profile and a higher residual mass, which is consistent with the presence of the inorganic LDH phase and the formation of inorganic oxide/hydroxide residue after thermal treatment. The DSC curve does not contain sharp, well-resolved peaks that could be assigned to individual reactions. Instead, the broad DSC response reflects overlapping thermal processes accompanying degradation of the organic chitosan matrix and transformation of the inorganic LDH component.

We also used ICP analysis for a primary assessment of the amount of the Mg–Fe LDH component in the chitosan/Mg–Fe LDH composite. The Mg and Fe contents were 0.74 wt.% and 0.86 wt.%, respectively, corresponding to a Mg/Fe molar ratio of 1.98, which is close to the expected 2:1 ratio for Mg_2Fe-LDH. Since the formation of the LDH phase was confirmed by X-ray diffraction and no separate crystalline Mg- or Fe-containing phases were detected, these ICP data were used to calculate the LDH-equivalent content. Assuming the formation of $[Mg_2Fe(OH)_6](NO_3) \times nH_2O$, the composite contains approximately 4.1 wt.% of anhydrous Mg–Fe LDH equivalent, or approximately 4.5–5.0 wt.% when interlayer/structural water is considered.

The chitosan/Mg–Fe LDH composite is intrinsically heterogeneous because it consists of an organic chitosan matrix and an inorganic LDH phase. Therefore, complete molecular-level homogeneity cannot be expected for this type of material. However, the heterogeneity of the composite can be controlled at the preparation stage by maintaining fixed synthesis parameters, including the chitosan/Mg/Fe ratio, Mg/Fe precursor ratio, rate of alkali addition, stirring intensity, washing procedure, and drying conditions. In the present synthesis, NaOH was added dropwise under vigorous stirring and pulsed ultrasound treatment. These conditions were used to promote the in situ formation of small Mg–Fe LDH particles and their distribution within the precipitating chitosan matrix. As a result, the obtained composite was macroscopically homogeneous, while XRD and FTIR confirmed the formation of the LDH phase in the chitosan matrix. Batch-to-batch reproducibility of such composites can be monitored by ICP analysis of Mg and Fe contents, Mg/Fe molar ratio, characteristic LDH reflections in XRD, FTIR bands of the LDH component, and sorption performance.

3.4. Sorption Equilibria Study

The sorption properties of the prepared composite toward hexavalent chromium (chromate anions) were assessed by studying sorption equilibria. We also compared the sorption capacity of the composite with that of the starting chitosan and “pure” magnesium–iron LDH. Fixed volumes of potassium chromate solutions with concentrations increasing

from 0.04046 to 2.1577 g/L were added to the same amount of the sorbent. Upon reaching sorption equilibrium, we determined the equilibrium chromate concentration (C_e) and calculated the equilibrium adsorption value (q_e). Figure 9 displays the adsorption isotherm as a function of q_e versus C_e.

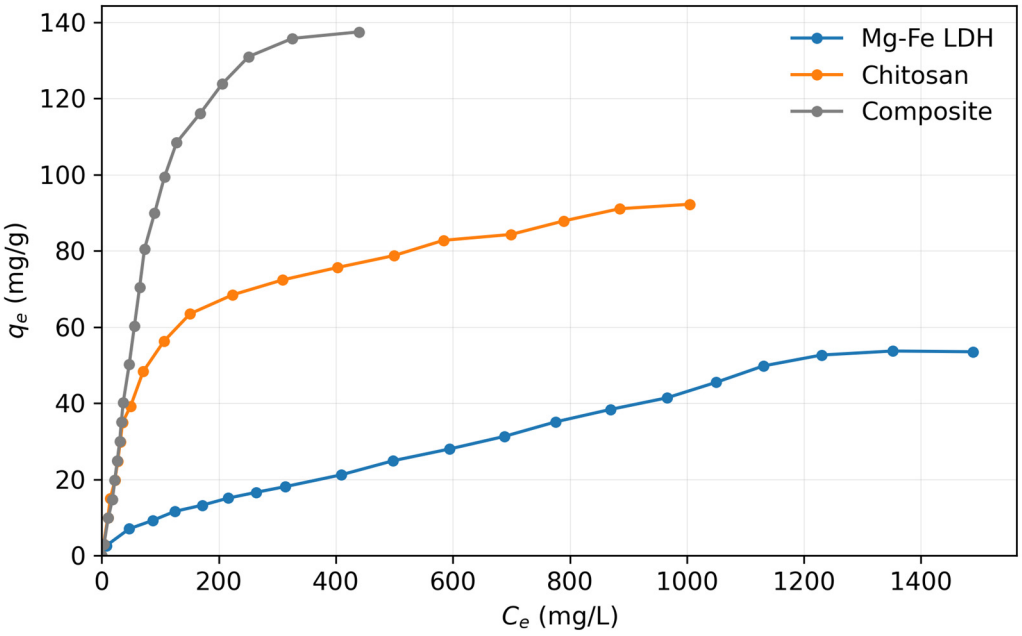


Figure 9. Experimental adsorption isotherms of chromate anions by magnesium–iron LDH, chitosan, and the chitosan/Mg–Fe LDH composite.

An increase in the equilibrium chromate concentration results in an increase in the adsorption value, which gradually reaches a plateau. The experimental plateau adsorption capacity, $Q_{plateau,exp}$, was defined as the equilibrium adsorption value q_e reached in the plateau region of the experimentally measured adsorption isotherm. This value was calculated from the mass-balance equation described in Section 2 and should not be confused with a model-derived Langmuir parameter. The $Q_{plateau,exp}$ values were 137.4 mg/g for the synthesized chitosan/Mg–Fe LDH composite, 92.2 mg/g for chitosan, and 53.5 mg/g for magnesium–iron LDH. Thus, chitosan is a more effective sorbent than LDH, while the introduction of LDH into the chitosan polymer matrix results in the formation of a composite with a sorption capacity almost 50% greater than that of the starting chitosan.

These findings are consistent with recently reported data, where the authors demonstrated that the phenol sorption capacity increases in the series NiAl LDH–chitosan–Chitosan@NiAl LDH [56]. However, the main difference in their work is in the method for producing the composite: the authors used the classical two-stage method, as described above in the Introduction. In our work, we propose a one-step method for synthesizing a chitosan–LDH composite (see Section 3.3).

We analyzed the obtained equilibrium data using the classical Langmuir and Freundlich isotherms. The Langmuir isotherm is derived under specific assumptions, including adsorption on energetically equivalent sites and monolayer surface coverage. In contrast, the Freundlich isotherm is an empirical equation commonly used to describe adsorption on heterogeneous surfaces.

The Langmuir and Freundlich isotherm parameters were estimated by nonlinear least-squares fitting in the original q_e versus C_e coordinates. Linearized forms were not used for parameter estimation, because different linear transformations of adsorption isotherms

lead to different optimization targets and may distort the statistical weight of experimental points. For both isotherms, the same objective function was minimized:

$$SSE = \Sigma_i\ w_i(q_{e,i}(exp) - q_{e,i}(calc))^2,$$

where $q_{e,i}(exp)$ and $q_{e,i}(calc)$ are the experimental and calculated equilibrium adsorption values, respectively. Equal weights were used for all experimental points ($w_i = 1$), and the same weighting scheme was applied to both the Langmuir and Freundlich isotherms. The quality of fitting was evaluated using the residuals calculated in the original q_e scale; RMSE and R^2 values are reported as additional descriptive statistics.

The Langmuir isotherm was written as:

$$q_e = Q_l K_l C_e/(1 + K_l C_e),$$

where Q_l is the fitted Langmuir maximum adsorption parameter and K_l is the Langmuir affinity constant. The Freundlich isotherm was written as:

$$q_e = K_F\ C_e\ ^{(1/n)},$$

where K_F is the Freundlich constant and $1/n$ is the heterogeneity parameter. The fitted curves are shown in Figures 10 and 11, and the corresponding parameters are summarized in Table 3. It should be emphasized that $Q_{plateau,exp}$ is the experimentally observed plateau adsorption capacity, whereas Q_l is a fitted Langmuir parameter; therefore, these values should not be used interchangeably.

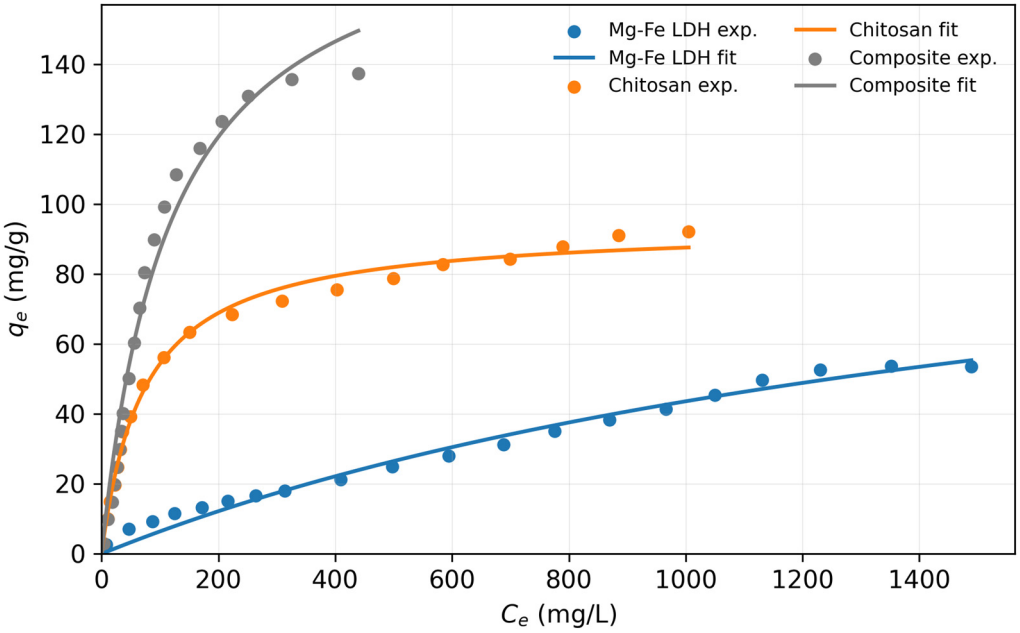


Figure 10. Experimental adsorption isotherms and nonlinear Langmuir fits for chromate adsorption by magnesium–iron LDH, chitosan, and the chitosan/Mg–Fe LDH composite.

The nonlinear fitting results show that the suitability of the isotherms depends on the sorbent. For magnesium–iron LDH, the Freundlich isotherm provides the better description in the studied concentration range (RMSE = 1.61 mg/g, R^2 = 0.9912) compared with the Langmuir isotherm (RMSE = 2.21 mg/g, R^2 = 0.9835). For chitosan and the chitosan/Mg–Fe LDH composite, the Langmuir isotherm provides the better description: for chitosan, RMSE = 2.44 mg/g and R^2 = 0.9936 for Langmuir versus RMSE = 6.58 mg/g and R^2 = 0.9534 for Freundlich; for the composite, RMSE = 7.02 mg/g and R^2 = 0.9770 for Langmuir versus

RMSE = 13.76 mg/g and R^2 = 0.9114 for Freundlich. Thus, the adsorption by magnesium–iron LDH is better described by the Freundlich isotherm, whereas adsorption by chitosan and the chitosan/Mg–Fe LDH composite is better described by the Langmuir isotherm under the conditions used in this study.

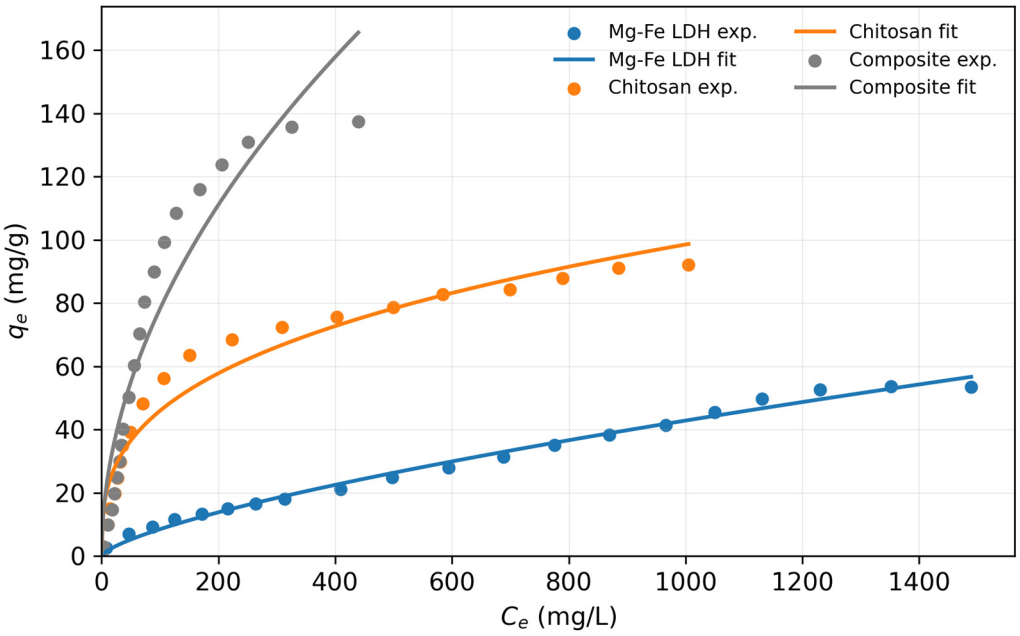


Figure 11. Experimental adsorption isotherms and nonlinear Freundlich fits for chromate adsorption by magnesium–iron LDH, chitosan, and the chitosan/Mg–Fe LDH composite.

Table 3. Parameters of Langmuir and Freundlich fitting in the original q_e versus C_e coordinates.

Sample	$Q_{plateau,exp}$, mg/g	Langmuir Model				Freundlich Model			
		Q_l, mg/g	K_l, L/mg	RMSE, mg/g	KF	1/*n*	RMSE, mg/g	R^2	KF
Mg-Fe LDH	53.5	122.9	0.00055	2.21	0.9835	0.334	0.703	1.61	0.9912
Chitosan	92.2	94.0	0.0137	2.44	0.9936	9.98	0.331	6.58	0.9534
Composite	137.4	190.0	0.00844	7.02	0.9770	7.57	0.507	13.76	0.9114

The Freundlich $1/n$ values are lower than 1 for all three sorbents, which is consistent with heterogeneous adsorption surfaces. The heterogeneity is expected for these systems since the composite combines both an organic polymer matrix and an inorganic LDH phase. The surface heterogeneity is a characteristic feature of the composite material rather than an indication of uncontrolled synthesis. Its degree is governed by the distribution of LDH particles in the chitosan matrix and can be minimized by controlling the coprecipitation conditions.

The relatively high concentration range used in the equilibrium adsorption experiments was selected intentionally to construct complete adsorption isotherms and reach the plateau region required for estimating the experimental adsorption capacity. These experiments were aimed at comparing the sorption capacities of the studied materials and fitting adsorption isotherms, rather than directly reproducing the concentration level of natural waters. The performance of the composite under more environmentally relevant conditions was evaluated separately in simulated groundwater containing competing inorganic anions.

3.5. Kinetics Studies

Along with sorption capacity, sorption rate is another important parameter of sorbent effectiveness. Sorbents with the highest sorption capacity typically have the highest sorption rate, but this relationship is not absolute. Therefore, each new sorbent should be studied not only in terms of sorption equilibria (a suitable model for describing the equilibria and experimentally determined sorption capacity) but also in terms of the kinetics of the sorption process (kinetics equation and rate constant). In this study, we evaluated the kinetics of the sorption process for three tested sorbents by quantifying the change in the adsorption value q_t over time (Figure 12).

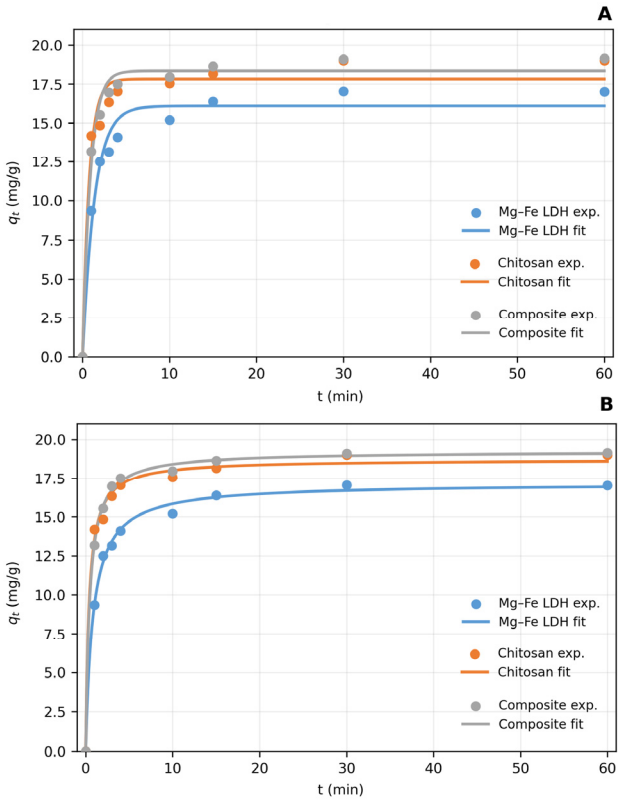


Figure 12. Experimental sorption kinetic curves and nonlinear kinetic fits for chromate adsorption by magnesium–iron LDH, chitosan, and the chitosan/Mg–Fe LDH composite: (**A**) pseudo-first-order equation and (**B**) pseudo-second-order equation.

The kinetic curves (Figure 12) for all tested sorbents show the absence of an induction period. Three main regions can be distinguished for each sorbent: (1) a very rapid increase in adsorption during the first minutes of contact, (2) a slower increase in q_t as the system approaches equilibrium, and (3) a plateau region. After 60 min, the experimental adsorption values were 17.03 mg/g for magnesium–iron LDH, 19.00 mg/g for chitosan, and 19.15 mg/g for the chitosan/Mg–Fe LDH composite. Thus, the adsorption value reached after 60 min increases in the series Mg–Fe LDH < chitosan < chitosan/Mg–Fe LDH composite.

The kinetic data were analyzed using the pseudo-first-order and pseudo-second-order kinetic equations. The parameters were estimated by nonlinear least-squares fitting in the original q_t versus t coordinates. Linearized forms were not used for parameter estimation, because different linear transformations of kinetic equations lead to different optimization targets and may distort the statistical weight of experimental points.

For both kinetic equations, the same objective function was minimized:

$$SSE = \Sigma_i \, w_i(q_{t,i}(exp) - q_{t,i}(calc))^2,$$

where $q_{t,i}$(exp) and $q_{t,i}$(calc) are the experimental and calculated adsorption values at time t_i, respectively. Equal weights were used for all experimental points ($w_i = 1$), and the same weighting scheme was applied to both kinetic equations. The fitting quality was evaluated using the residuals calculated in the original q_t scale; RMSE and R^2 values are reported as descriptive statistics.

The pseudo-first-order equation was written as:

$$q_t = q_e(1 - \exp^{-k_1 t}),$$

where q_e is the fitted equilibrium adsorption value and k_1 is the pseudo-first-order rate constant. The pseudo-second-order equation was written as:

$$q_t = k_2 q_e^2 t/(1 + k_2 q_e t),$$

where k_2 is the pseudo-second-order rate constant. The fitted curves are shown in Figure 12, and the corresponding kinetic parameters are summarized in Table 4.

Table 4. Nonlinear fitting parameters for pseudo-first-order and pseudo-second-order kinetic equations.

Sample	q_t,60, mg/g	Pseudo-First-Order Equation				Pseudo-Second-Order Equation			
		q_e(calc.), mg/g	k_1, min^{-1}	RMSE, mg/g	R^2	q_e(calc.), mg/g	k_2, g mg^{-1} min^{-1}	RMSE, mg/g	R^2
Mg-Fe LDH	17.03	16.10	0.7193	0.84	0.9728	17.16	0.06954	0.30	0.9965
Chitosan	19.00	17.82	1.3084	0.99	0.9683	18.72	0.13749	0.46	0.9932
Composite	19.15	18.34	1.1131	0.65	0.9872	19.24	0.11448	0.20	0.9987

The nonlinear fitting results show that the pseudo-second-order equation provides a better description of the chromate sorption kinetics for all tested sorbents. For magnesium–iron LDH, the pseudo-second-order equation gives RMSE = 0.30 mg/g and R^2 = 0.9965, compared with RMSE = 0.84 mg/g and R^2 = 0.9728 for the pseudo-first-order equation. For chitosan, RMSE decreases from 0.99 to 0.46 mg/g, and R^2 increases from 0.9683 to 0.9932 when the pseudo-second-order equation is used. For the chitosan/Mg–Fe LDH composite, the pseudo-second-order equation gives the lowest RMSE value among all fits (0.20 mg/g) and the highest R^2 value (0.9987).

The fitted q_e values obtained from the pseudo-second-order equation are also close to the adsorption values reached experimentally after 60 min: 17.16 versus 17.03 mg/g for Mg–Fe LDH, 18.72 versus 19.00 mg/g for chitosan, and 19.24 versus 19.15 mg/g for the composite. In contrast, the pseudo-first-order equation underestimates the equilibrium adsorption values and gives systematically larger residuals. Thus, chromate sorption kinetics by the studied sorbents are better described by the pseudo-second-order equation. The composite combines the highest adsorption amount reached within the experiment with fast approach to the plateau region.

To further analyze the possible contribution of diffusion processes to chromate uptake, the kinetic data were additionally treated using the Weber-Morris intraparticle diffusion equation:

$$q_t = k_i d\, t^{1/2} + C,$$

where k_id is the intraparticle diffusion rate constant and C is the intercept related to the boundary-layer effect. If intraparticle diffusion is the only rate-controlling step, the plot of q_t versus $t^{1/2}$ should be linear and pass through the origin. In the present case, the linear fitted portions of the plots did not pass through the origin and showed multi-stage behavior. This indicates that intraparticle diffusion contributes to the adsorption kinetics but is not

the sole rate-controlling process. The chromate uptake proceeds through a rapid initial surface adsorption stage, followed by a slower diffusion-related stage and subsequent approach to equilibrium (Figure 13).

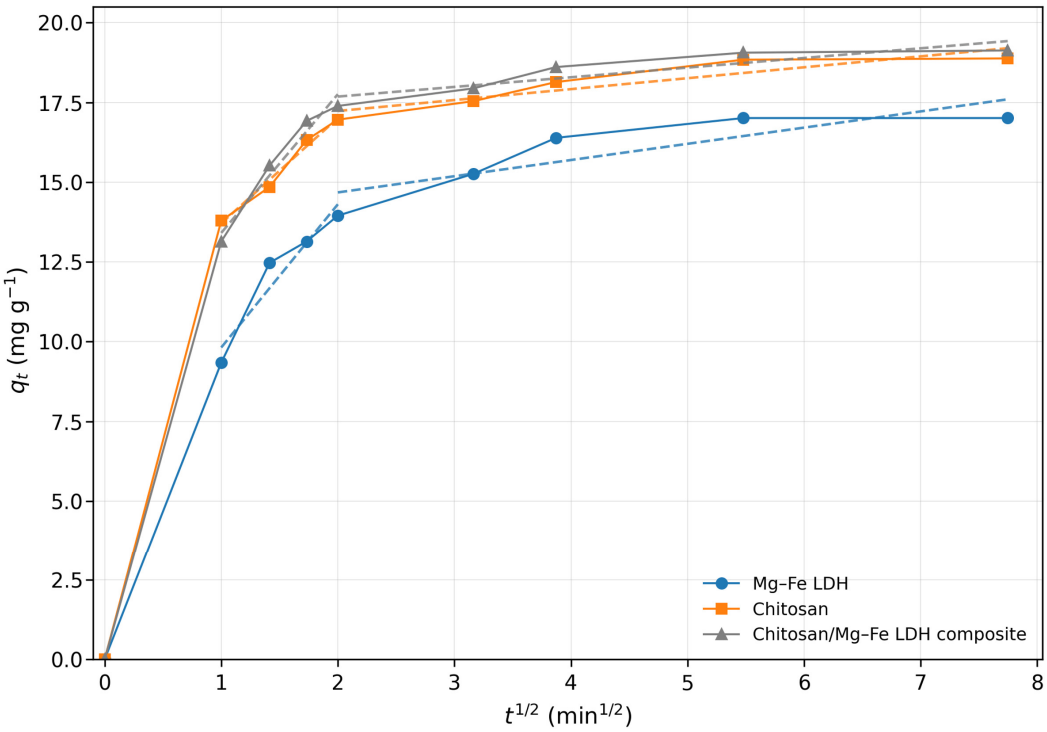


Figure 13. Weber-Morris intraparticle diffusion plots for chromate adsorption by magnesium–iron LDH, chitosan, and the chitosan/Mg–Fe LDH composite. Dashed lines show the linear fits for the two kinetic regions.

The Weber-Morris parameters (Table 5) confirm that chromate sorption proceeds through at least two kinetic regions.

Table 5. Weber-Morris fitting parameters for chromate adsorption kinetics.

Sorbent	Region	t Range (min)	k_id (mg g^{-1} min$^{-1/2}$)	C (mg/g)	R^2
Mg–Fe LDH	I	1–4	4.491	5.324	0.9192
Mg–Fe LDH	II	4–60	0.508	13.662	0.7436
Chitosan	I	1–4	3.299	10.410	0.9840
Chitosan	II	4–60	0.343	16.547	0.8448
Chitosan/Mg–Fe LDH composite	I	1–4	4.349	9.060	0.9624
Chitosan/Mg–Fe LDH composite	II	4–60	0.303	17.078	0.8147

In the initial region, the k_id values are considerably higher than in the later region, which is consistent with rapid uptake by readily accessible external surface sites. In the second region, the lower k_id values indicate slower diffusion-related uptake and gradual approach to equilibrium.

Thus, the Weber-Morris analysis supports a multistep adsorption mechanism. Since the fitted lines do not pass through the origin, intraparticle diffusion cannot be considered the only rate-controlling step for any of the studied sorbents. Instead, chromate adsorption is controlled by a combination of fast surface interaction/boundary-layer effects and

slower diffusion-related processes, which is consistent with the kinetic curves and with the nonlinear pseudo-second-order fitting discussed above.

3.6. Efficiency of the Studied Sorbents in Groundwater

In the previous stages of this study, we identified the highest sorption capacity for the chitosan/LDH composite and recognized it as the clear leader. However, chromate sorption from groundwater has a number of unique characteristics and is typically less efficient than chromate sorption from its solution in distilled water. This is because chromate sorption from groundwater is complicated by the presence of various competing anions (sulfates, bicarbonates, chlorides, etc.). We evaluated the sorption capacity of the prepared chitosan/LDH composite in simulated groundwater, i.e., water that, in addition to CrO_4^{2-} anions (10 mg/L), also contains Cl^- (100 mg/L), HCO_3^- (100 mg/L), and SO_4^{2-} (50 mg/L). Indeed, chromate anion sorption under these conditions should be significantly impaired, since the concentration of competing ions is 5–10 times higher than the concentration of CrO_4^{2-} anions. For control purposes, we accompanied sorption experiments with simulated groundwater with similar experiments using distilled water containing only CrO_4^{2-} anions (10 mg/L). The results demonstrating the difference in chromate sorption from distilled water, on the one hand, and from simulated groundwater, on the other, are summarized in Table 6.

Table 6. Efficiency of the tested sorbents in capturing chromate from groundwater.

Sample	Distilled H_2O Containing Chromate Anions			Simulated Groundwater		
	Tested sorbent content, g/L					
	0.20	0.50	1.00	0.20	0.50	1.00
	Chromate uptake, %					
LDH	50	77	100	14	21	31
Chitosan	73	96	100	25	34	52
Composite	79	100	100	31	55	82

The results displayed in Table 6 demonstrate that all tested sorbents are capable of capturing chromate anions not only from their solution in pure water but also from simulated groundwater, despite the latter having a concentration of competing anions up to 10 times higher than the concentration of hexavalent chromium.

In the case of capturing chromate ions from their solution in distilled water, we observed the following patterns. First, even the least effective sorbent (LDH), at its lowest concentration in the reaction mixture (0.20 g/L), is capable of capturing at least half of the hexavalent chromium. Furthermore, the low concentration of the sorbents (0.20 g/L) has a differential effect on their sorption capacity. The weakest sorbent (LDH) adsorbs 50% of chromate, while the more effective chitosan sorbent absorbs 1.46 times more chromate (chromate capture is 73%). The most effective sorbent (chitosan/LDH composite) absorbs 79% of chromate anions, which is 1.58 times higher than the corresponding result for pure LDH. In contrast, the high sorbent content (1.00 g/L) results in a leveling effect on their sorption effect: at a high sorbent concentration, their efficiency was maximum and ensured 100% capture of chromate anions.

In experiments with simulated groundwater, we observed significantly lower efficiency for all sorbents. Undoubtedly, the main reason for the decrease in sorption capacity is the presence of competing anions in concentrations higher than those of chromate [57]. However, the decrease in sorption capacity of the tested sorbents is not uniform. The greatest decrease in sorption capacity is observed for the least effective sorbent (LDH),

while the most effective sorbent (chitosan/LDH composite) reduces its sorption effect to a significantly lesser extent. For example, even at the highest (and therefore most favorable) sorbent concentration (1.00 g/L), the sorption effect in simulated groundwater decreases by 70% for LDH, by almost half for chitosan, and by only 18% for the chitosan/LDH composite. Based on the results of experiments with simulated groundwater, the chitosan/LDH composite is the clear leader and is capable of achieving the highest percentage of hexavalent chromium capture even under conditions of high concentrations of competing anions.

The simulated groundwater used in this work should be regarded as a simplified model system rather than a complete reproduction of real groundwater. Its main purpose was to evaluate the effect of common inorganic competing anions on chromate uptake. Therefore, the obtained results demonstrate the stability of chromate sorption in a competitive inorganic medium, while experiments with real groundwater samples containing natural organic matter and trace components should be considered as the next step toward practical validation.

3.7. Reusability of the Composite as a Chromate Sorbent

Effective composite sorbents are most attractive if they are recyclable. Recyclability is important for both environmental and industrial applications. Furthermore, recyclability allows not only for the removal of chromate from wastewater but also for its recovery and further concentration and use. In this study, we assessed the recyclability of the best-performing sorbent tested, i.e., chitosan/LDH composite. EDTA can typically be effectively used to remove chromate ions from chitosan-based sorbents. However, in this case, we consider this method impractical, as EDTA, a powerful chelator, can remove Mg^{2+} and Fe^{3+} ions from LDHs, thereby causing their partial destruction. Washing the sorbent with a strong acid also appears questionable, as the acid can not only disrupt the LDH structure but also lead to partial dissolution of the chitosan polymer matrix. We decided to remove chromate ions from the sorbent using a sodium hydroxide solution, which is safe for LDH and does not dissolve chitosan. Indeed, sodium hydroxide can cause minor deacetylation of chitosan, but under the experimental conditions, the probability of secondary deacetylation approaches zero. This is because more or less noticeable deacetylation is observed only at elevated temperatures, and at room temperature, this secondary process is dramatically slow.

In our experiments, we performed sorption cycles followed by desorption (Figure 14).

For sorption, we charged a vial with a K_2CrO_4 solution (10 mg/L) and the chitosan-LDH composite to achieve a concentration of 1.00 g/L. For desorption, we washed the sorbent with a 1 M NaOH solution.

The chitosan/LDH sorbent easily withstands five sorption/desorption cycles. During the first three cycles, chromate ion capture is exhaustive, reaching 100%. However, we did not observe complete chromate ion desorption: during the first three cycles, desorption slowly decreases from 97.3% to 94.3%. During the fourth and fifth cycles, a slightly greater decrease in desorption (to 90.3%) is observed; however, this does not affect the maintenance of 100% chromate ion sorption. These results demonstrate the pronounced recyclability of the chitosan/LDH composite.

The recyclability test was performed as a primary operational assessment rather than a full post-cycling structural stability study. The retained sorption performance indicates that NaOH regeneration restores the availability of sorption sites under the tested conditions. However, detailed post-cycle XRD, FTIR, and leaching analyses would be required to confirm structural and compositional stability after repeated use and will be addressed in future work.

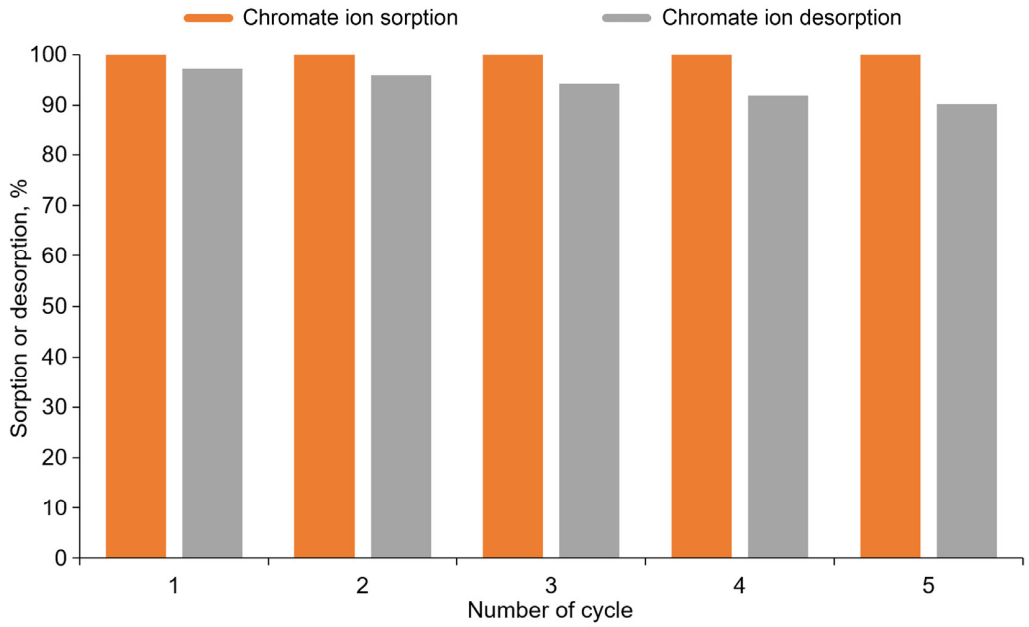


Figure 14. Results of reusability tests.

4. Conclusions

In this work, a chitosan/Mg–Fe layered double hydroxide composite was successfully prepared by a one-pot alkaline coprecipitation method, in which the LDH phase was generated in situ within the chitosan matrix. The formation of the composite was confirmed by XRD, FTIR, thermal analysis, and ICP data, which indicated an LDH-equivalent content of approximately 4.1 wt.% on an anhydrous basis.

The obtained composite showed improved chromate sorption performance compared with both pristine chitosan and Mg–Fe LDH. The experimental plateau adsorption capacity reached 137.4 mg/g, whereas chitosan and Mg–Fe LDH showed 92.2 and 53.5 mg/g, respectively. Nonlinear isotherm fitting demonstrated that chromate adsorption by Mg–Fe LDH was better described by the Freundlich model, while adsorption by chitosan and the composite was better described by the Langmuir model. Kinetic analysis showed that the sorption process followed the pseudo-second-order equation, and Weber–Morris analysis indicated a multistep uptake mechanism involving both surface interaction and diffusion-related processes.

The composite also demonstrated good performance in simulated groundwater containing competing anions, removing 82% of Cr(VI) at a sorbent dosage of 1.0 g/L. In addition, it retained complete chromate uptake over five sorption/desorption cycles, although the desorption efficiency gradually decreased from 97.3% to 90.3%.

Overall, the proposed one-pot strategy provides a simple route to chitosan/LDH composite sorbents with enhanced chromate removal ability. However, further studies using real contaminated water samples, dynamic flow systems, extended cycling tests, and metal-leaching analysis are required to confirm the practical applicability and long-term stability of the material.

Author Contributions: Conceptualization, R.A.G., A.S.K. and O.M.K.; methodology, R.A.G., A.R.E., D.I.S., L.V.N. and N.N.L.; software, N.N.L.; validation, A.G.T., A.A.K. and W.L.; formal analysis, G.Z.M.; investigation, R.A.G. and O.M.K.; resources, N.N.L.; data curation, A.V.K. and L.V.N.; writing—original draft preparation, R.A.G., A.S.K., A.R.E., D.I.S. and L.V.N.; writing—review and editing, A.A.K., N.N.L., A.G.T., G.Z.M., A.V.K., W.L. and O.M.K.; visualization, D.I.S. and G.Z.M.; supervision, A.S.K., A.G.T. and W.L.; project administration, A.A.K., W.L. and O.M.K.; funding acquisition, A.R.E. All authors have read and agreed to the published version of the manuscript.

Funding: The study was supported by the Russian Science Foundation grant № 25-73-00229, https://rscf.ru/en/project/25-73-00229/ (accessed on 18 May 2026).

Institutional Review Board Statement: Not applicable.

Data Availability Statement: The original contributions presented in this study are included in the article. Further inquiries can be directed to the corresponding author(s).

Conflicts of Interest: The authors declare no conflicts of interest.

References

1. Delbianco, M.; Seeberger, P.H. Materials science based on synthetic polysaccharides. *Mater. Horiz.* **2020**, *7*, 963–969. [CrossRef]
2. Torres, F.G.; Troncoso, O.P.; Urtecho, A.; Soto, P.; Pachas, B. Recent Progress in Polysaccharide-Based Materials for Energy Applications: A Review. *ACS Appl. Mater. Interfaces* **2025**, *17*, 13179–13196. [CrossRef] [PubMed]
3. Jain, R.; Singhal, N.; Vardhan, H.; Vashistha, P.; Bist, Y.; Pandey, A.; Wagri, N.K.; Gaur, A. Polysaccharide-based functional materials for flexible electronics: A comprehensive review of synthesis strategies, functionalization, and applications. *Carbohydr. Polym. Technol. Appl.* **2025**, *12*, 101038. [CrossRef]
4. Salvay, A.G. Polysaccharide-Based Materials: Developments and Properties. *Polymers* **2025**, *17*, 3028. [CrossRef]
5. Harugade, A.; Sherje, A.P.; Pethe, A. Chitosan: A review on properties, biological activities and recent progress in biomedical applications. *React. Funct. Polym.* **2023**, *191*, 105634. [CrossRef]
6. Mishra, G.; Dash, B.; Pandey, S. Layered double hydroxides: A brief review from fundamentals to application as evolving biomaterials. *Appl. Clay Sci.* **2018**, *153*, 172–186. [CrossRef]
7. Altalhi, A.A.; Mohamed, E.A.; Negm, N.A. Recent advances in layered double hydroxide (LDH)-based materials: Fabrication, modification strategies, characterization, promising environmental catalytic applications, and prospective aspects. *Energy Adv.* **2024**, *3*, 2136–2151. [CrossRef]
8. Xu, H.; Yao, B. Industrial applications of layered double hydroxide (LDH) catalysts in high-current density water electrolysis. *Int. J. Hydrogen Energy* **2025**, *162*, 150714. [CrossRef]
9. Kritchenkov, A.S.; Bokach, N.A.; Starova, G.L.; Kukushkin, V.Y. A palladium(II) Center activates nitrile ligands toward 1,3-dipolar cycloaddition of nitrones substantially more than the corresponding platinum(II) center. *Inorg. Chem.* **2012**, *51*, 11971–11979. [CrossRef] [PubMed]
10. Bolotin, D.S.; Bokach, N.A.; Kritchenkov, A.S.; Haukka, M.; Kukushkin, V.Y. Amidrazone complexes from a cascade platinum(II)-mediated reaction between amidoximes and dialkylcyanamides. *Inorg. Chem.* **2013**, *52*, 6378–6389. [CrossRef]
11. Shivakumar, M.T.; Jayaram, S.; Kenchegowda, M.; Osmani, R.A.M.; Rahamathulla, M.; Palaksha, S.; Yadav, R.H.; Gangadharappa, H.V. Layered double hydroxides based nanomaterials: Recent advances in drug delivery and biomedical applications. *Health Nanotechnol.* **2025**, *1*, 18. [CrossRef]
12. Zhu, Y.; Zhu, R.; Chen, Q.; Laipan, M.; Zhu, J.; Xi, Y.; He, H. Calcined Mg/Al layered double hydroxides as efficient adsorbents for polyhydroxy fullerenes. *Appl. Clay Sci.* **2018**, *151*, 66–72. [CrossRef]
13. Semenov, K.N.; Charykov, N.A.; Keskinov, V.A.; Kritchenkov, A.S.; Murin, I.V. Fullerenol-d solubility in fullerenol-d-inorganic salt-water ternary systems at 25 °C. *Ind. Eng. Chem. Res.* **2013**, *52*, 16095–16100. [CrossRef]
14. Singh, D.; Das, A.K. In Situ Fabricated Small Organic Molecule-Anchored Bimetallic Hydroxide-based Nanohybrids for Symmetric Supercapacitor. *Energy Fuels* **2022**, *36*, 13317–13326. [CrossRef]
15. Singh, D.; Wagh, L.; Das, A.K. Multifunctional benzoselenadiazole-capped organic molecule-based nanohybrid for efficient asymmetric supercapacitor and oxygen evolution reaction. *J. Energy Storage* **2024**, *104*, 114604. [CrossRef]
16. Pellanda, A.C.; Neto, A.G.C.; Carvalho Jorge, A.R.D.; Berton, M.A.C.; Floriano, J.B.; Thomas, S.; Vijayan, P.P. Performance Evaluation of Layered Double Hydroxides Containing Benzotriazole and Nitrogen Oxides as Autonomic Protection Particles against Corrosion. *Int. J. Polym. Sci.* **2021**, *2021*, 6630194. [CrossRef]
17. Grudova, M.V.; Kubasov, A.S.; Khrustalev, V.N.; Novikov, A.S.; Kritchenkov, A.S.; Nenajdenko, V.G.; Borisov, A.V.; Tskhovrebov, A.G. Exploring Supramolecular Assembly Space of Cationic 1,2,4-Selenodiazoles: Effect of the Substituent at the Carbon Atom and Anions. *Molecules* **2022**, *27*, 1029. [CrossRef] [PubMed]
18. Dong, L.; Shan, C.; Liu, Y.; Sun, H.; Yao, B.; Gong, G.; Jin, X.; Wang, S. Characterization and Mechanistic Study of Heavy Metal Adsorption by Facile Synthesized Magnetic Xanthate-Modified Chitosan/Polyacrylic Acid Hydrogels. *Int. J. Environ. Res. Public Health* **2022**, *19*, 11123. [CrossRef]
19. Alhalili, Z.; Abdelrahman, E.A. Efficient removal of Zn(II) ions from aqueous media using a facilely synthesized nanocomposite based on chitosan Schiff base. *Sci. Rep.* **2024**, *14*, 17598. [CrossRef]

20. Al-Ahmed, Z.A.; Alhasani, M.; Aljohani, M.M.; Snari, R.M.; Alghasham, H.A.; Alatawi, N.M.; Keshk, A.A.; El-Metwally, N.M. Facile synthesis of new metal-organic framework/chitosan composite sponge for Hg(II) removal: Characterization, adsorption efficiency, and optimization using Box-Behnken design. *Int. J. Biol. Macromol.* **2024**, *259*, 129282. [CrossRef]
21. Chimprasit, A.; Hannongbua, S.; Saparpakorn, P. Adsorption study of lac dyes with chitosan coated on silk fibroin using molecular dynamics simulations. *J. Mol. Graph. Model.* **2021**, *106*, 107934. [CrossRef] [PubMed]
22. Nizam, N.U.M.; Hanafiah, M.M.; Mahmoudi, E.; Halim, A.A.; Mohammad, A.W. The removal of anionic and cationic dyes from an aqueous solution using biomass-based activated carbon. *Sci. Rep.* **2021**, *11*, 8623. [CrossRef]
23. Dinu, I.A.; Ghimici, L.; Răschip, I.E. Macroporous 3D Chitosan Cryogels for Fastac 10EC Pesticide Adsorption and Antibacterial Applications. *Polymers* **2022**, *14*, 3145. [CrossRef]
24. Musarurwa, H.; Tavengwa, N.T. Advances in the application of chitosan-based metal organic frameworks as adsorbents for environmental remediation. *Carbohydr. Polym.* **2022**, *283*, 119153. [CrossRef]
25. Gama, B.M.V.D.; Selvasembian, R.; Giannakoudakis, D.A.; Triantafyllidis, K.S.; McKay, G.; Meili, L. Layered Double Hydroxides as Rising-Star Adsorbents for Water Purification: A Brief Discussion. *Molecules* **2022**, *27*, 4900. [CrossRef] [PubMed]
26. Cherepakhina, E.S.; Logachev, D.A.; Ryabinkin, R.A.; Godzishevskaya, A.A.; Kurasova, M.N.; Rubanik, V.V.; Rubanik, V.V., Jr.; Khrustalev, V.N.; Kirichuk, A.A.; Mammadova, G.Z.; et al. Synthesis and adsorption properties of Al–Zn and Al–Ni layered double hydroxides. *Mendeleev Commun.* **2026**, *36*, 92–94. [CrossRef]
27. Li, M.; Dopilka, A.; Kraetz, A.N.; Jing, H.; Chan, C.K. Layered Double Hydroxide/Chitosan Nanocomposite Beads as Sorbents for Selenium Oxoanions. *Ind. Eng. Chem. Res.* **2018**, *57*, 4978–4987. [CrossRef]
28. Grover, A.; Mohiuddin, I.; Malik, A.K.; Aulakh, J.S.; Kukkar, D.; Kim, K.H. Chitosan-Ni/Fe layered double hydroxide composites as an efficient solid phase extraction sorbent for HPLC-PDA monitoring of parabens in personal care products. *Chemosphere* **2021**, *264*, 128429. [CrossRef] [PubMed]
29. Yang, B.; Liu, J.; Liu, Z.; Wang, Y.; Cai, J.; Peng, L. Preparation of chitosan/Co-Fe-layered double hydroxides and its performance for removing 2,4-dichlorophenol. *Environ. Sci. Pollut. Res.* **2019**, *26*, 3814–3822. [CrossRef]
30. Mohadi, R.; Siregar, P.M.S.B.N.; Palapa, N.R.; Taher, T.; Lesbani, A. Layered Double Hydroxide/Chitosan Composite (Mg-Al/CT) as a Selective Adsorbent in Congo Red Adsorption from Aqueous Solution. *Ecol. Eng. Environ. Tech.* **2022**, *23*, 144–152. [CrossRef]
31. Abdel-Hady, E.E.; Hafez, S.H.M.; Mohamed, H.F.M.; Elsharkawy, M.R.M. Characterization and application of LDH with chitosan composites investigated by positron annihilation lifetime spectroscopy and surface texture for the adsorption of methyl orange. *Sci. Rep.* **2024**, *14*, 16501. [CrossRef]
32. Huang, Z.; Xiong, C.; Ying, L.; Wang, W.; Wang, S.; Ding, J.; Lu, J. Facile synthesis of a MOF-derived magnetic CoAl-LDH@chitosan composite for Pb (II) and Cr (VI) adsorption. *Chem. Eng. J.* **2022**, *449*, 137722. [CrossRef]
33. Lyu, F.; Yu, H.; Hou, T.; Yan, L.; Zhang, X.; Du, B. Efficient and fast removal of Pb 2+ and Cd 2+ from an aqueous solution using a chitosan/Mg-Al-layered double hydroxide nanocomposite. *J. Colloid Interface Sci.* **2019**, *539*, 184–193. [CrossRef] [PubMed]
34. Palapa, N.R.; Yuliasari, N.; Siregar, P.M.S.B.N.; Wijaya, A.; Amri, A.; Ahmad, N.; Lesbani, A. Selective Adsorption of Direct Group Anionic Dyes on Layered Double Hydroxide-Chitosan Composites. *Bull. Chem. React. Eng. Catal.* **2023**, *18*, 37–47. [CrossRef]
35. Fei, C.; Chen, C.; Zhang, H.; Liu, A.; Ju, D.; Yang, X.; Wang, F.; Xia, M.; Huang, P. The effective removal of Congo red dye via chitosan-layered double hydroxide composite and the deep insight into mechanism. *J. Ind. Eng. Chem.* **2024**, *135*, 143–153. [CrossRef]
36. Siddiq, H.A.; Madkhali, M.M.M.; Ghubayra, R.; Alaghaz, A.N.M.A.; El-Desouky, M.G.; El-Bindary, M.A.; El-Bindary, A.A. Efficient removal of tetracycline by VCo-layered double hydroxide encapsulated with chitosan: Optimization via Box-Behnken design, and thermodynamics. *Int. J. Biol. Macromol.* **2025**, *296*, 139565. [CrossRef] [PubMed]
37. AlSalem, H.S.; Alatawi, R.A.S.; Bukhari, A.A.H.; Alnawmasi, J.S.; Zghab, I.; El-Desouky, M.G.; Almabadi, M.H.; Alnakhli, Z.H.; Elsayed, N.H. Adsorption and removal of Pb (II) via layer double hydroxide encapsulated with chitosan; synthesis, characterization adsorption isotherms, kinetics, thermodynamics, & optimization via Box-Behnken design. *Int. J. Biol. Macromol.* **2024**, *283*, 137517. [CrossRef]
38. Ren, J.; Zhang, S.; Wang, Y.; Shi, H.; Zhen, C. Cr(VI) Adsorption by Mg/Al Layered Double Hydroxide-Modified Sphagnum Moss Cellulose Gel: Performance and Mechanism. *Molecules* **2025**, *30*, 1796. [CrossRef]
39. He, W.; Ye, K.; Zhang, M.; Bai, S.; Xu, S.; Fang, K. Enhanced Cr(vi) removal by Co and PPy co-modified Ca-Al-layered double hydroxides due to adsorption and reduction mechanisms. *RSC Adv.* **2024**, *14*, 37933–37948. [CrossRef]
40. Golubev, R.A.; Egorov, A.R.; Sikaona, N.D.; Esakova, V.E.; Semenkova, D.I.; Liu, W.; Khrustalev, V.N.; Kirichuk, A.A.; Maharramov, A.M.; Nazarov, R.H.; et al. Ultrasonic treatment and sorption properties of Mg^{2+}/Fe^{3+} layered double hydroxides. *Mendeleev Commun.* **2025**, *35*, 577–579. [CrossRef]
41. Vogel, A.I. *Vogel's Textbook of Macro and Semimicro Qualitative Inorganic Analysis*; Longman Group Limited: New York, NY, USA, 1979.
42. Lima Júnior, R.N.; Almeida, J.L.I.O.; de Andrade, J.; Abreu, F.O.M.S. Chitosan and carboxymethylchitosan as high turbidity water biocoagulants. *J. Renew. Mater.* **2020**, *8*, 1489–1504. [CrossRef]

43. Boymirzaev, A.S.; Berdimbetova, G.E.; Karlybaeva, B.P. Exclusion liquid chromatography of carboxymethylchitin and carboxymethylchitosan from crustacean Artemia Parthenogenetica of the Aral Sea. *Proc. Natl. Acad. Sci. Belarus Chem. Ser.* **2024**, *60*, 45–52. [CrossRef]
44. Brugnerotto, J.; Lizardi-Mendoza, J.; Goycoolea, F.M.; Argüelles-Monal, W.; Desbriéres, J.; Rinaudo, M. An infrared investigation in relation with chitin and chitosan characterization. *Polymer* **2001**, *42*, 3569–3580. [CrossRef]
45. Wang, W.; Bo, S.; Li, S.; Qin, W. Determination of the Mark-Houwink equation for chitosans with different degrees of deacetylation. *Int. J. Biol. Macromol.* **1991**, *13*, 281–285. [CrossRef]
46. Hirai, A.; Odani, H.; Nakajima, A. Determination of degree of deacetylation of chitosan by 1H NMR spectroscopy. *Polym. Bull.* **1991**, *26*, 87–94. [CrossRef]
47. Lim, S.H.; Hudson, S.M. Synthesis and antimicrobial activity of a water-soluble chitosan derivative with a fiber-reactive group. *Carbohydr. Res.* **2004**, *339*, 313–319. [CrossRef] [PubMed]
48. Lipin, V.A.; Gorkina, T.E. *Theoretical and Experimental Research Methods in Polymer Chemistry*; VShTE SPbGUPTD: St. Petersburg, Russia, 2021; p. 69.
49. Morsy, M.; Mostafa, K.M.; Ameen, H.A.M.; El Ebissy, A.A.H.; Hebishy, A.M.; Youssef, M.A. Synthesis and characterization of freeze dryer chitosan nanoparticles as multifunctional eco-friendly finish for fabricating easy care and antibacterial cotton textiles. *Egypt. J. Chem.* **2019**, *62*, 1277–1293.
50. Golban, A.; Lupa, L.; Cocheci, L.; Pode, R. Synthesis of mgfe layered double hydroxide from iron-containing acidic residual solution and its adsorption performance. *Crystals* **2019**, *9*, 514. [CrossRef]
51. Moussout, H.; Ahlafi, H.; Aazza, M.; Bourakhouadar, M. Kinetics and mechanism of the thermal degradation of biopolymers chitin and chitosan using thermogravimetric analysis. *Polym. Degrad. Stab.* **2016**, *130*, 1–9. [CrossRef]
52. de Britto, D.; Campana-Filho, S.P. Kinetics of the thermal degradation of chitosan. *Thermochim. Acta* **2007**, *465*, 73–82. [CrossRef]
53. Corazzari, I.; Nisticò, R.; Turci, F.; Faga, M.G.; Franzoso, F.; Tabasso, S.; Magnacca, G. Advanced physico-chemical characterization of chitosan by means of TGA coupled on-line with FTIR and GCMS: Thermal degradation and water adsorption capacity. *Polym. Degrad. Stab.* **2015**, *112*, 1–9. [CrossRef]
54. Neto, C.G.T.; Giacometti, J.A.; Job, A.E.; Ferreira, F.C.; Fonseca, J.L.C.; Pereira, M.R. Thermal analysis of chitosan based networks. *Carbohydr. Polym.* **2005**, *62*, 97–103. [CrossRef]
55. Shamim, M.; Dana, K. Thermal decomposition of layered double hydroxides: Kinetic modeling and validation. *Thermochim. Acta* **2016**, *632*, 64–71. [CrossRef]
56. Utami, H.P.; Ahmad, N.; Zahara, Z.A.; Lesbani, A.; Mohadi, R. Green Synthesis of Nickel Aluminum Layered Double Hydroxide using Chitosan as Template for Adsorption of Phenol. *Sci. Technol. Indones.* **2022**, *7*, 530–535. [CrossRef]
57. Kim, Y.; Son, Y.; Bae, S.; Kim, T.H.; Hwang, Y. Particle size and interlayer anion effect on chromate adsorption by MgAl-layered double hydroxide. *Appl. Clay Sci.* **2022**, *225*, 106552. [CrossRef]

Disclaimer/Publisher's Note: The statements, opinions and data contained in all publications are solely those of the individual author(s) and contributor(s) and not of MDPI and/or the editor(s). MDPI and/or the editor(s) disclaim responsibility for any injury to people or property resulting from any ideas, methods, instructions or products referred to in the content.